



Analysis of Radial Electromagnetic Force and Vibration Characteristics of Permanent-Magnet-Based Synchronous Motor for Vibration Management

Daolu Li¹ · Ying Xie¹ · Wei Cai¹ · Peng Chen¹

Received: 15 October 2022 / Revised: 18 February 2023 / Accepted: 5 May 2023 / Published online: 30 May 2023
© Krishtel eMaging Solutions Private Limited 2023

Abstract

Purpose This paper comprehensively analyses the radial electromagnetic (EM) force by unit area and vibration characteristics in a permanent magnet synchronous motor (PMSM). This provides the possibility to verify the action law, causes, and influencing factors of vibration deformation and provides new ideas for vibration management.

Methods Analytical and finite-element (FE) methods are utilized to deduce the spatial–temporal distribution of radial electromagnetic force and determine the force wave order with significant influence. Accordingly, the air-gap permeance is simplified as the superposition of constant and first-order variable permeance, and the air-gap flux density is regarded as spatial discretization and time continuity. After double equivalence, a theoretical analysis model is established, which is suitable for PMSM with the clogged stator, smooth rotor surface (CSSR) and smooth stator surface, and clogged rotor (SSCR). This model is utilized to analyze the vibration characteristics of the motor, including the deformation law.

Results The deformation law is in good agreement with FE analysis and experimental data, demonstrating the rationality of the hypothesis and the correctness of the theoretical analysis model.

Conclusions The theoretical analysis model shows that the motor deformation is mainly attributed to the total concentrated force and additional bending moment and is related to slot/pole combinations and pole-arc coefficient, which lays the foundation for vibration reduction.

Keywords Permanent magnet synchronous motor · Vibration characteristics · Deformation · Radial electromagnetic force · Bending moment · Theoretical analysis

Introduction

Due to its substantial benefits, such as simple structure, lightweight, high-power factor and high efficiency, permanent magnet synchronous motor (PMSM) has broad application prospects in various fields. However, this also puts higher requirements for motor operation [1–3]. As one of the critical performance indices, vibration and noise issues have gradually become a research hotspot and have aroused extensive attention [4]. In the preliminary stage of motor design, parameters and excitation source design are closely related to vibration and noise level. An unreasonable design

scheme is responsible for severe vibration and noise problems, degrading the motor's efficiency. Therefore, it is crucial to discuss the noise excitation source of PMSM and related issues to improve motor performance [5–7].

Motor vibration mainly includes mechanical, aerodynamic and electromagnetic (EM) vibration. Since the radial EM force in the air-gap periodically deforms the stator core, this paper only concentrates on EM vibration caused by the interaction of radial EM force in the air-gap [8, 9]. Consequently, research on radial EM force and stator core deformation is the premise of motor vibration further analysis, revealing the inherent law of motor vibration and fundamentally realizing vibration and noise reduction.

Radial EM force is the dominating source of vibration. The analytical method was adopted in [10] to calculate the no-load magnetic field, armature reaction magnetic field, stator slotting magnetic field, and load magnetic field of surface-mounted PMSM, laying the foundation for radial EM

✉ Ying Xie
xieying_1975@163.com

¹ School of Electrical and Electronic Engineering, Harbin University of Science and Technology, Harbin, China

force calculation. Then, the fast Fourier analysis method was employed to establish the relationship between frequency and order of radial EM force and illustrate the critical role of the spatial–temporal distribution [11]. The existing force analysis usually ignores the influence of tangential force, and the nonuniformly distributed radial EM force is equivalent to a concentrated force acting on the tooth center for calculation [12, 13]. This method does not consider additional bending moment contributed by the nonuniformly distributed force, inducing extra error. Meanwhile, in the spatial–temporal distribution of the radial EM force, the influence of the specific order force on vibration has been extensively studied [14–17]. Lin et al. [18] deduced the lowest spatial order force by an analytical model considering current harmonics and explained its influence on motor vibration and noise peak. Yang et al. [19] demonstrated that the force harmonics with low modal order could generate significant mechanical vibration. In [20], the relationship between the zero-order mode and lowest non-zero-order mode and the vibration was revealed based on the time variation of the spatial force distribution mean. However, there is a lack of research on the impact of specific order radial force on the total concentrated force and total additional bending moment.

These is a specific deformation law under the action of time-varying radial EM force called the vibration mode. Depending on the fixed support beam displacement equation, vibration mode directly determines the vibration amplitude, affecting the sound pressure level (SPL). Thus, in-depth research should be performed on the vibration mode to analyze the vibration and noise [21]. In [22], the vibration modes and excitation frequencies with different slot/pole combinations were converted into SPL for noise comparison. In [23–25], the motor vibration law was extensively studied under different conditions. In the existing stator vibration mode analysis, although more emphasis has been placed on noise prediction or influence, there is little research on the causes. Wang et al. [26] illustrated the causes of vibration mode through PMSM with a smooth stator surface and cogged rotor (SSCR) under the no-load condition. However, the analysis method could not be applied to PMSM with the cogged stator and smooth rotor surface (CSSR).

This paper presents a detailed analysis of the radial EM force by unit area and determines the low spatial order force wave that significantly influences the motor. The above conclusion is employed to establish a double equivalent model of air-gap permeance and air-gap flux density. It mainly comprises total concentrated force and additional bending moment applicable to PMSM with SSCR or CSSR. Besides, it can be utilized to analyze the action law, causes, and influencing factors of stator vibration mode. Taking an interior PMSM with a rated power of 3 kW with CSSR as the research object, the finite-element (FE) and experimental

Table 1 Basic parameters

Parameter	Value
Rated power	3 kW
Rated voltage	380 V
Rated speed	750 rpm
Stator slots number	36
Poles-pairs	3
Stator outer diameter	210 mm
Air-gap length	1 mm

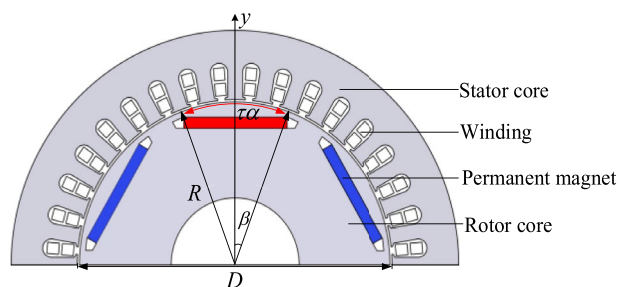


Fig. 1 Two-dimensional FE model

methods are employed to verify the radial EM force wave distribution and deformation law.

Study on Radial EM Force Wave with Significant Influence on Motor

The radial EM force wave comprises components with different frequencies and amplitudes. The components with low-order and high-amplitude characteristics are more likely to contribute significantly to vibration and noise levels. Besides, resonance will occur when the radial EM force wave frequencies are close to the modal frequencies. In this section, the radial EM force wave with significant influence can be acquired through spatial order, amplitude, and modal frequencies.

Basic Parameters and the FE Model

Taking an I-shaped interior PMSM with a rated power of 3 kW with CSSR as the research object, the basic parameters are shown in Table 1, and the two-dimensional FE model is shown in Fig. 1.

Analytical and FE Analysis of Radial EM Force Wave with Low Spatial Order

Since the core permeability is much larger than the air gap, the tangential component of the EM force wave is much

smaller than the radial one and can be neglected [27]. Thus, the EM force wave can be expressed as:

$$p_r(\theta, t) \approx \frac{b_r^2(\theta, t)}{2\mu_0} = \frac{[f(\theta, t)\lambda(\theta, t)]^2}{2\mu_0}, \tag{1}$$

where $b_r(\theta, t)$ is radial air-gap flux density, μ_0 is the vacuum permeability, $f(\theta, t)$ is the air-gap magnetic motive force (MMF), $\lambda(\theta, t)$ is air-gap permeance, θ is the mechanical angle, and t is time.

When the motor is in no-load condition, the permanent magnet (PM) provides the following air-gap MMF:

$$f_1(\theta, t) = \sum_{\mu} F_{\mu} \cos\left(\frac{\mu\omega_1}{p}t - \mu\theta\right), \tag{2}$$

where p is the number of pole-pairs, μ is the order of rotor harmonics, $\mu = (2r + 1)p$, $r = 0, 1, 2, \dots$, F_{μ} is the amplitude of MMF, which is related to the air-gap flux density amplitude B_{μ} and the air-gap length δ , and can be expressed as $F_{\mu} = B_{\mu}\delta/\mu_0$, and ω_1 is the fundamental angular frequency.

When the motor is in rated-load condition, the following air-gap MMF is mainly provided by the PM and armature winding:

$$f_2(\theta, t) = f_1(\theta, t) + \sum_{\nu} F_{\nu} \cos(\omega_1 t - \nu\theta + \varphi_{\nu}), \tag{3}$$

where ν is the order of stator harmonics, which are related to number of slots per pole and per phase q , when q is an integer, $\nu = (6k + 1)p$, $k = 0, \pm 1, \pm 2, \pm 3, \dots$, and φ_{ν} is the initial phase angle of the air-gap MMF.

Assuming that the rotor has no eccentricity and a smooth surface, the air-gap permeance is expressed as:

$$\lambda(\theta, t) = \Lambda_0 + \sum_{k=1}^{\infty} \Lambda_k \cos(kZ_1\theta), \tag{4}$$

where Λ_0 is the constant component of air-gap permeance, Λ_k is the amplitude of the k th harmonic permeance, and Z_1 is the stator slots number.

According to [27], taking μ_0/δ as the base value, the air-gap permeance can be further expressed as:

$$\lambda'(\theta, t) = \frac{\mu_0}{\delta} \Lambda_0^* + \sum_{k=1}^{\infty} (-1)^{k+1} \frac{\mu_0}{\delta} \Lambda_k^* \cos(kZ_1\theta). \tag{5}$$

After sorting out Eqs. (1, 2, 3, 4, 5), the spatial–temporal distribution of radial EM force wave in no-load condition can be obtained, as shown in Table 2 as A–E, and the one in the rated-load condition is shown as A–I. Since the low spatial order in the spatial–temporal distribution significantly influences the motor, this part focuses on the analysis. When the motor is in no-load condition, the radial EM force wave can be classified into two types according to origin: one

Table 2 Spatial–temporal distribution of radial EM force wave

Symbol	Spatial order	Temporal order
A	2μ	$2\mu/p$
B	$\mu_2 \pm \mu_1$	$(\mu_2 \pm \mu_1)/p$
C	$2(\mu \pm kZ_1)$	$2\mu/p$
D	$(\mu_2 \pm \mu_1) \pm (k_2 \pm k_1)Z_1$	$(\mu_2 \pm \mu_1)/p$
E	$\mu_2 \pm \mu_1 \pm kZ_1$	$(\mu_2 \pm \mu_1)/p$
F	$\mu \pm \nu$	$(\mu \pm p)/p$
G	$\mu \pm \nu \pm kZ_1$	$(\mu \pm p)/p$
H	2ν	2
I	$\nu_1 + \nu_2$	2

contributed by the main pole magnetic field and the other modulated by the tooth harmonic magnetic field, which are A, B and C, D, E, respectively. The spatial–temporal distribution of A and B are $(2\mu, 2\mu/p)$, $[\mu_2 \pm \mu_1, (\mu_2 \pm \mu_1)/p]$, respectively, and can be further expressed as $[2(2r + 1)p, 2(2r + 1)]$ and $[(2r_2 + 1)p \pm (2r_1 + 1)p, (2r_2 + 1) \pm (2r_1 + 1)]$. When $r = 0$, $r_2 - r_1 = 1$, the $(2p, 2)$ with low spatial order emerges. The low spatial orders of C, D, and E are generated by the interaction between the rotor main pole magnetic field ($\mu = p$) and the tooth harmonic magnetic field ($k = 1$), which are expressed as $r = \mu \pm (p \pm Z_1) = (2r + 1)p \pm (p \pm Z_1)$. When the two “ \pm ” take different signs, the r expression reaches the minimum recorded as r_3 and r_4 , and the corresponding frequencies are f_{r_3} and f_{r_4} , respectively:

$$r_3 = \mu - (p + Z_1) = 2rp - Z_1, f_{r_3} = 2rf, \tag{6}$$

$$r_4 = \mu + (p - Z_1) = 2(r + 1)p - Z_1, f_{r_4} = 2(r + 1)f. \tag{7}$$

When the motor is in rated-load condition, the spatial orders μ include all spatial orders $|\nu|$, so the spatial orders $\mu \pm \nu$, 2ν , $\nu_1 + \nu_2$ are all within the range of 2μ , and orders $\mu \pm \nu \pm kZ_1$ are all within the range of $\mu_2 \pm \mu_1 \pm kZ_1$. Accordingly, the low spatial orders of radial EM force wave are precisely the same under no-load and rated-load conditions, and the corresponding spatial–temporal distribution is $(2p, 2)$, $(2rp - Z_1, 2r)$, and $[2(r + 1)p - Z_1, 2(r + 1)]$. Thus, the spatial–temporal distribution with low spatial orders of the 36-slot/6-pole combination can be arranged as $(6, 2)$ and $(0, 12)$, where $k = 1$, $r = 5$ or $r = 6$.

FE analysis is performed on the no-load and rated-load conditions to further verify the rationality of analytical derivation. When the motor runs at a steady state, each position's radial air-gap flux density at every moment is substituted into Eq. (1). Figure 2 shows the radial EM force wave curves, and Fig. 3 shows the spatial–temporal characteristics obtained by the Fourier decomposition.

As shown in Fig. 3, the spatial–temporal characteristics show the parallel diagonal distribution, in which the

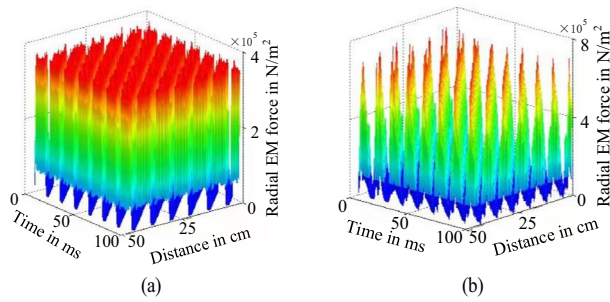


Fig. 2 Radial EM force wave curves under **a** no-load condition and **b** rated-load condition

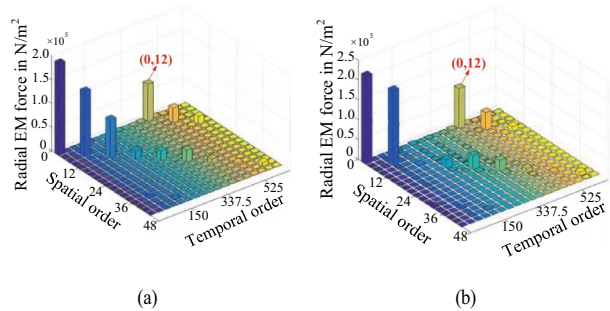


Fig. 3 The spatial–temporal characteristics of radial EM force wave under **a** no-load condition and **b** rated-load condition

corresponding orders of the main pole magnetic field and the tooth harmonic magnetic field are (6, 2), (12, 4), (18, 6), (24, 8), (30, 10), (36, 12) and (0, 12), (6, 14), (12, 16), which is consistent with Table 4. Furthermore, the force amplitude of (6, 2) and (0, 12) is more prominent. (0, 12) is mainly generated by the interaction between the main pole magnetic field and the first-order tooth harmonic. The amplitude is more significant than other tooth harmonics and is dominant in tooth harmonics.

Modal Analysis

As the rotor and shaft have little influence on modal results, the established three-dimensional prototype model only includes the enclosure, end covers, stator core and winding. Nevertheless, the meshing quality of winding is poor in the FE analysis, leading to a considerable error. Therefore, appropriate simplifications are necessary for the modal analysis; that is, the winding of the loose wire and its end is equivalent to a bar and an end ring, respectively. Figure 4 shows the prototype model of 36-slot/6-pole and each component.

Assuming that the equivalent winding mass is equal to the actual mass, and the equivalent density is the ratio of mass

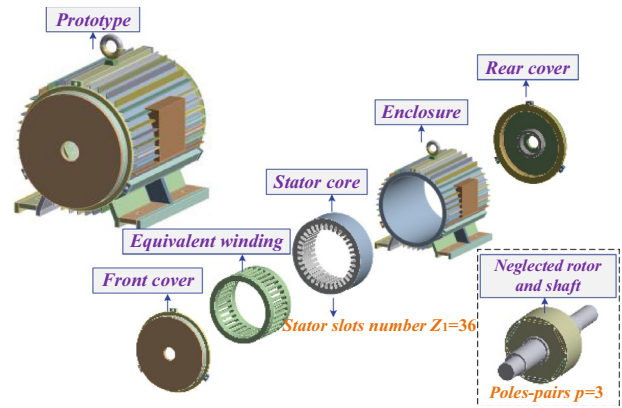


Fig. 4 Prototype model of 36-slot/6-pole and each component

to equivalent volume, the elastic modulus can be calculated by slot fill factor and insulating material. Partial material parameters are presented in Table 3.

Material parameters in Table 3 are added to the prototype, and the modal results are shown in Fig. 5. The second-order and third-order modal frequencies are 1015.1 Hz and 2267.1 Hz, respectively, which are far away from the force wave frequencies with significant influence on the motor so that no resonance will occur. Consider that the force wave frequencies with significant influence can be obtained from the temporal orders of (6,2) and (0,12), which are $2f=75$ Hz and $12f=450$ Hz, respectively.

Noise Calculation

The prototype under no-load and rated-load conditions is applied to attain multi-speed effective radiation power level curves, as shown in Fig. 6a and b.

Figure 6 shows an apparent bright line in the 36th order, indicating its most contribution to the total SPL. The noise order is equal to the ratio of frequency to rotation frequency, and the rotation frequency is revolutions per second. At 750 rpm, the rotation frequency is 12.5 Hz, so the frequency corresponding to the 36th order is 450 Hz, which corresponds to $12f$ of the radial EM force wave. Therefore, the spatial–temporal distribution (0, 12) can lead to more severe vibration and noise, and at this time, $k=1$.

Analysis of Stator Vibration Mode

Theoretical Analysis of the Vibration Mode

The vibration mode analysis is based on Fig. 1, where the stator inner radius is R , and the calculated polar distance is $\tau\alpha$, where τ is the polar distance, α is the polar arc coefficient, and β is a central angle expressed as follows:

Table 3 Partial material parameters of the prototype

Attribute	Enclosure, end cover	Core	Equivalent winding
Material	Cast iron	50W470	Copper
Density (kg·m ⁻³)	7000	7305	5800
Elastic modulus (Pa)	1.25E+11	2.05E+11	1.20E+9
Poisson ratios	0.25	0.3	0.3

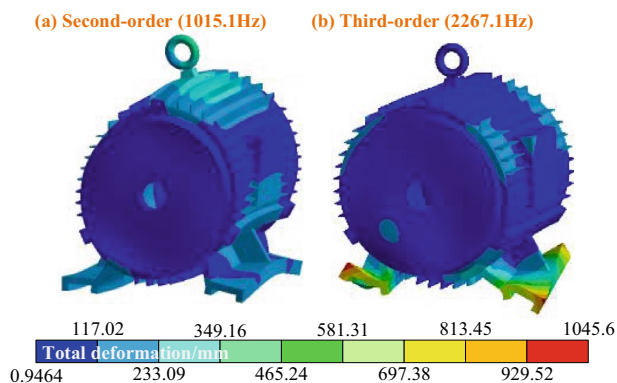


Fig. 5 The second-order and third-order modal frequencies and modal shapes

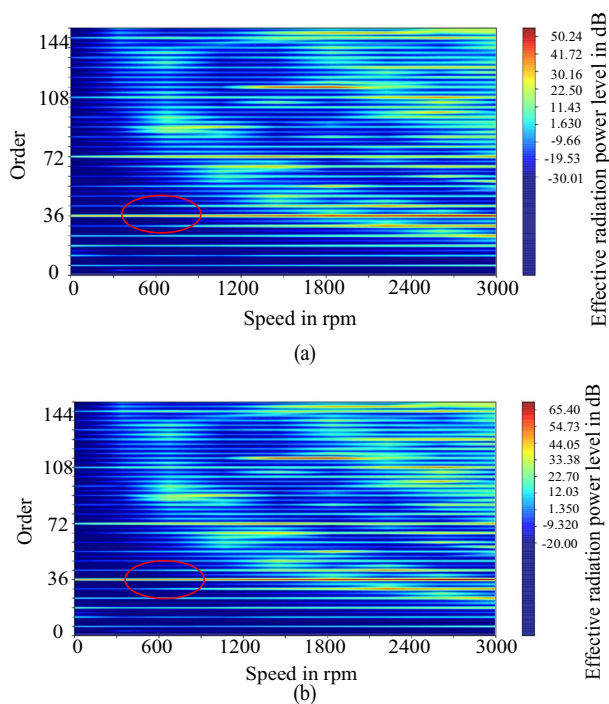


Fig. 6 Effective radiation power level curves under **a** no-load condition and **b** rated-load condition

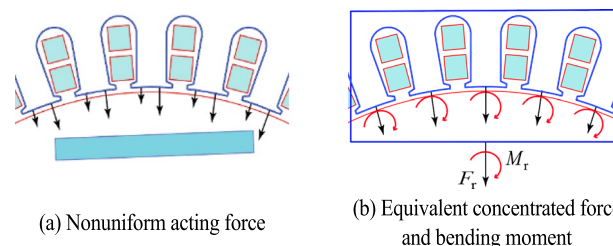


Fig. 7 The **a** nonuniform acting force and **b** equivalent concentrated force and bending moment

$$\beta = \frac{\frac{\tau\alpha}{2}}{R} = \frac{\frac{\pi D\alpha}{2p \times 2}}{R} = \frac{\alpha\pi}{2p} \tag{8}$$

As shown in Fig. 7a, the radial EM force on each stator tooth has a nonuniform amplitude. For calculation convenience, the force on each tooth is equivalent to a concentrated force and an additional bending moment, as shown in Fig. 7b. The tooth corresponding to one pole is equivalent to a total concentrated force F_r and a total additional bending moment M_r by ignoring the slotted effect. This will be introduced in depth later.

Double equivalence is required before discussing the stator vibration mode:

- (1) As described in the previous section, when $k = 1$, the radial EM force significantly influences the vibration. Thus, Eq. (4) can only be considered as the superposition of constant and first-order tooth harmonic permeances, and the expression is:

$$\lambda'(\theta, t) = \Lambda_0 + \Lambda_1 \cos(Z_1\theta), \tag{9}$$

where Λ_1 is the first-order tooth harmonic permeance.

- (B) The air-gap flux density is a function of time and space. It is discretized in space and continuous in time to simplify the calculation. Also, it is equivalent to a square wave after ignoring the slotted effect in space, whose height is B_δ and width is $\tau\alpha$, as shown in Fig. 8. After determining the spatial impact, the relationship between the air-gap flux density and time can be approximated with a cosine function. The polar coordinate system is established with the vertical y direction of Fig. 1 as the 0-degree reference direction.

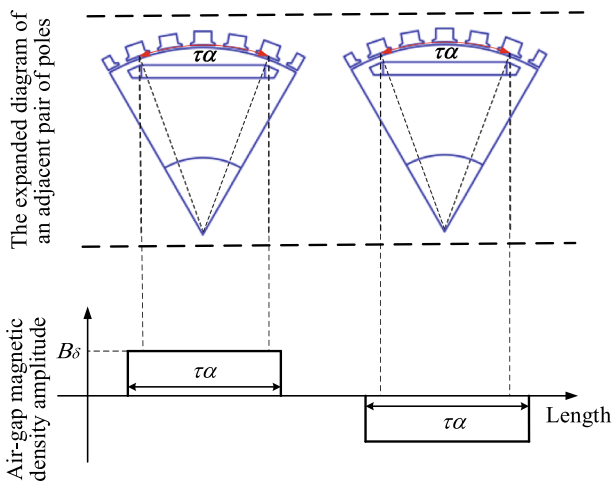


Fig. 8 The spatial impact on air-gap flux density

According to Fig. 1 and Fig. 8, the cosine relationship can be expressed as follows:

$$B = \begin{cases} B_\delta \cos \omega t \left[-\beta + i\frac{2\pi}{2p}, \beta + i\frac{2\pi}{2p} \right] & i = 2m \\ 0 \left[\beta + i\frac{2\pi}{2p}, -\beta + (i+1)\frac{2\pi}{2p} \right] & i = n \\ -B_\delta \cos \omega t \left[-\beta + i\frac{2\pi}{2p}, \beta + i\frac{2\pi}{2p} \right] & i = 2m + 1 \end{cases}$$

$$m = 0, 1, 2 \quad n = 0, 1, 2, 3, 4, 5 \quad (10)$$

where B is the equivalent air-gap flux density under the action of time and space, and ω is the angular frequency.

In the above equivalence, the calculation of air-gap permeance only considers the dominant harmonic. The air-gap flux density calculation ignores the slotted effect to realize waveform idealization. The two-point equivalent methods have little effect on the vibration amplitude and do not affect the vibration mode.

According to Eqs. (1, 2, 3, 5) and (8, 9, 10), the actual air-gap flux density can be expressed as:

$$b'_r(\theta, t) = F_\delta \cos \omega t \times (\Lambda_0 + \Lambda_1 \cos Z_1 \theta) = B_\delta \Lambda_0^* \cos \omega t + \frac{1}{2} B_\delta \Lambda_1^* \cos(Z_1 \theta \pm \omega t), \quad (11)$$

where F_δ is the amplitude of MMF corresponding to the equivalent air-gap flux density.

By substituting Eq. (11) into Eq. (1), the actual radial EM force wave is:

$$p'_r(\theta, t) = \left[\frac{\Lambda_0^{*2} \cos^2 \omega t}{2\mu_0} + \frac{\Lambda_1^{*2} \cos^2(Z_1 \theta \pm \omega t)}{8\mu_0} + \frac{\Lambda_0^* \Lambda_1^* \cos(Z_1 \theta \pm \omega t)}{2\mu_0} \right] \times B_\delta^2. \quad (12)$$

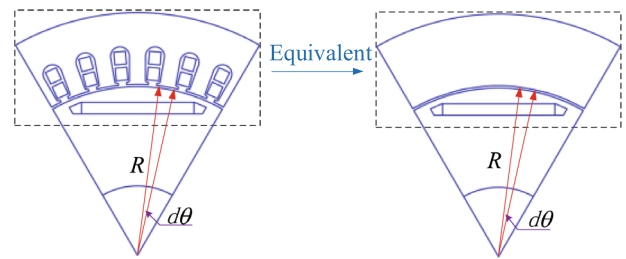


Fig. 9 Equivalent integral diagram

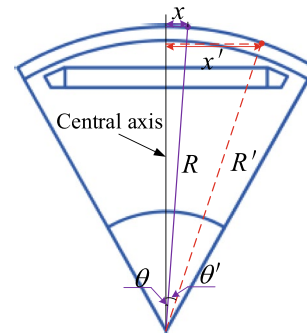


Fig. 10 The action mode of the force arm

The first two terms in Eq. (12) are small and can be ignored. Considering only the influence of the third term, Eq. (12) can be expressed as:

$$p'_{r1}(\theta, t) = \frac{B_\delta^2 \Lambda_0^* \Lambda_1^*}{2\mu_0} \cos(Z_1 \theta \pm \omega t). \quad (13)$$

Regardless of the stator slotted effect, considering the teeth corresponding to one pole, the F_r of this part can be calculated by integrating the radial EM force wave at a certain point. The equivalent integral diagram is shown in Fig. 9 ($d\theta$ is the unit angle), and the calculation formula is:

$$F_r = l_p \int_{-\frac{\alpha_1}{2p} + i\frac{2\pi}{2p}}^{\frac{\alpha_1}{2p} + i\frac{2\pi}{2p}} p'_{r1}(\theta, t) R d\theta = \frac{l_p B_\delta^2 \Lambda_0^* \Lambda_1^* R}{\mu_0 Z_1} \sin \alpha_1 \pi \cos(i2\pi Z_p \pm 2\omega t), \quad (14)$$

where l_p is the magnetic pole length, $\alpha_1 = \alpha Z_1 / 2p$, and $Z_p = Z_1 / 2p$.

The M_r also plays an essential role in the vibration mode, which can be acquired by multiplying the force by the force arm. The force expression is shown in Eq. (14).

The force arm x (or x') is expressed as the distance from any action point to the central axis in Eq. (15), and the action mode is illustrated in Fig. 10.

$$x = R \sin \theta \text{ (or } x' = R' \sin \theta'). \tag{15}$$

By sorting out Eqs. (14) and (15), M_r can be expressed as follows:

$$M_r = l_p \int_{-\frac{\alpha\pi}{2p} + i\frac{2\pi}{2p}}^{\frac{\alpha\pi}{2p} + i\frac{2\pi}{2p}} P'_{r1}(\theta, t) x dx \tag{16}$$

$$= \frac{l_p B_\delta^2 \Lambda_0^* \Lambda_1^* R^2}{2\mu_0 Z_1} \sin \frac{\alpha\pi}{2p} \cos \alpha_1 \pi \sin(i2\pi Z_p \pm \omega t).$$

Equations (14) and (16) show that the amplitude of F_r is twice that of M_r , both of which are sine and cosine functions and are all affected by $l_p, B_\delta, \Lambda_0^*, \Lambda_1^*, R, Z_1, Z_p$, etc. Among them, the sine relation $\sin \alpha_1 \pi$ and the cosine relation $\cos \alpha_1 \pi$ significantly influence F_r and M_r , respectively, and so does Z_p . Based on the sine and cosine characteristics, α_1 can be divided into integer and (integer + 0.5). Z_p represents the stator teeth number under each magnetic pole. When integer teeth are included, the force arms on both sides are equal because the distance between each tooth under the left and right polar arcs and centerline is equal. The bending moment phases on the teeth corresponding to adjacent magnetic poles are also consistent. When (integer + 0.5) teeth are included, the phases are opposite. When α_1 is an integer or (integer + 0.5) and Z_p is an integer or (integer + 0.5), the action law of F_r and M_r can be expressed as follows:

- (1) When Z_p and α_1 are both integers, the bending moments on the teeth corresponding to adjacent magnetic poles are in phase, the F_r is the smallest, and the M_r is the largest. The vibration mode is $2p$, as shown in Fig. 11a.
- (2) When Z_p is an integer, and α_1 is (integer + 0.5), the bending moments on the teeth corresponding to adjacent magnetic poles are in phase, the M_r is the smallest, and the F_r is the largest. The vibration mode is 0, as shown in Fig. 11b.
- (3) When Z_p is (integer + 0.5), and α_1 is an integer, the bending moments on the teeth corresponding to adjacent magnetic poles have opposite phases, the F_r is the smallest, and the M_r is the largest. The vibration mode is p , as shown in Fig. 11c.
- (4) When Z_p and α_1 are both (integer + 0.5), the bending moments on the teeth corresponding to adjacent magnetic poles have opposite phases, the M_r is the smallest, and the F_r is the largest. The vibration mode is p , as shown in Fig. 11d.

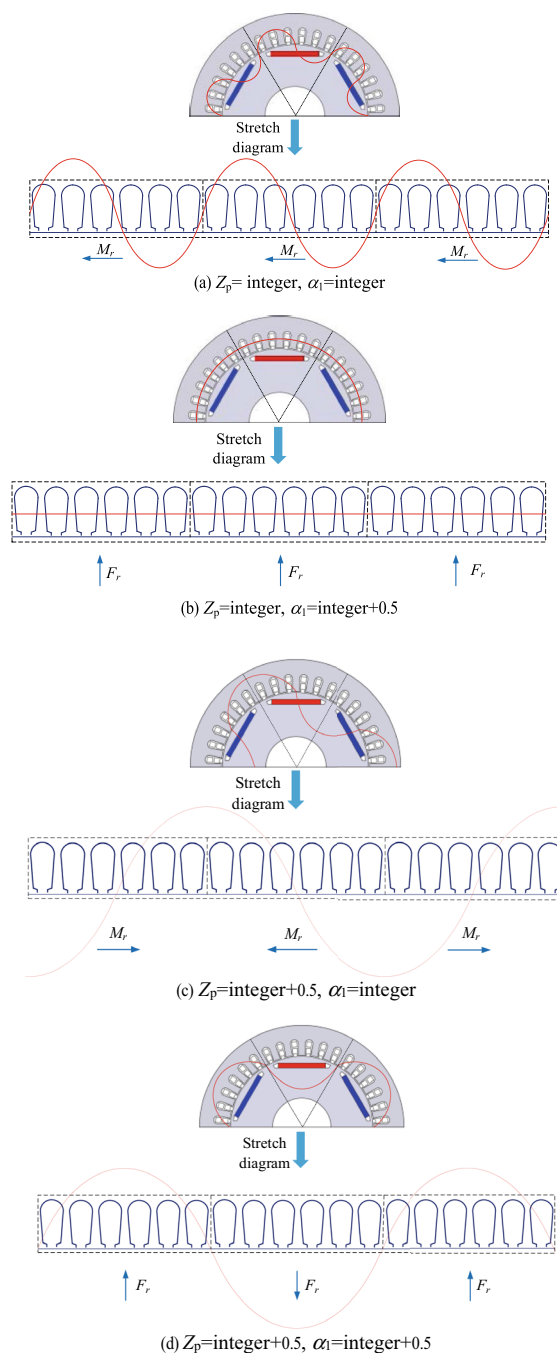


Fig. 11 The stator vibration modes under four cases: a Z_p =integer, α_1 =integer, b Z_p =integer, α_1 =integer+0.5, c Z_p =integer+0.5, α_1 =integer, and d Z_p =integer+0.5, α_1 =integer+0.5

The vibration mode law in four cases can be summarized in Table 4. Table 4 shows that the vibration mode is determined by the cooperation of bending moment phase direction and excitation source attribute, determined by Z_p and α_1 , respectively. Since $Z_p = Z_1/2p$ and $\alpha_1 = \alpha Z_1/2p$, the two are mainly affected by slot/pole combination, which is critical to stator vibration mode.

Table 4 The vibration mode law of stator core

Z_p	Bending moment phase direction	α_1	Excitation source attribute	Vibration mode
Integer	Same	Integer	M_r	$2p$
		Integer + 0.5	F_r	0
Integer + 0.5	Opposite	Integer	M_r	p
		Integer + 0.5	F_r	p

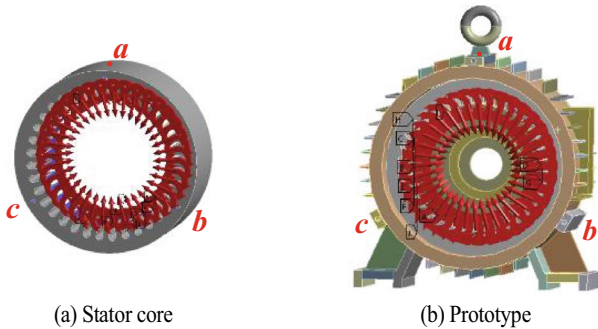


Fig. 12 FE model of **a** stator core and **b** prototype

The above scheme employs the double equivalent method to analyze the causes and influencing factors of the vibration mode of PMSM with CSSR. This method can simplify the calculation and clarify the relationship between slot/pole combination and vibration mode. For PMSM with SSCR, the air-gap permeance is presented in Eq. (17). After applying the double equivalent method, the expression of F_r' is shown in Eq. (18). This has only a phase change compared to the original F_r , while M_r is the same as the change. The phenomenon shows that the stator vibration mode law in Table 4 is satisfied. Thus, this scheme applies to PMSM with CSSR and PMSM with SSCR.

$$\lambda''(\theta, t) = \Lambda_0 + \Lambda_1 \cos(Z_2\theta - Z_2\Omega_2 t), \tag{17}$$

where Z_2 is the rotor slots number, and Ω_2 is the rotor mechanical angular velocity.

$$F_r' = \frac{l_p B_\delta^2 \Lambda_0^* \Lambda_1^* R}{\mu_0 Z_1} \sin \alpha_1 \pi \cos(i2\pi Z_p \pm 2\omega t - Z_2 \Omega_2 t). \tag{18}$$

FE Simulation of the Vibration Mode

The radial EM force gained by two-dimensional FE analysis under no-load and rated-load conditions is circularly loaded on the stator core and the prototype, as shown in Fig. 12. In the model of Fig. 12a, 120° symmetrical bolt holes on the stator yoke are set, and cylindrical constraints

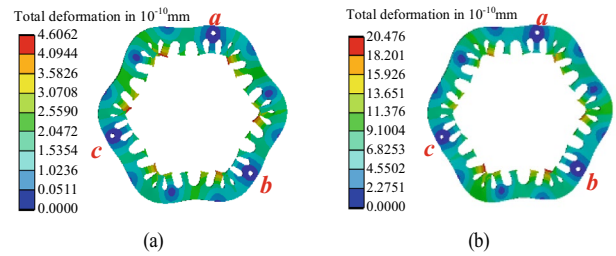


Fig. 13 Stator vibration modes under **a** no-load condition and **b** rated-load condition

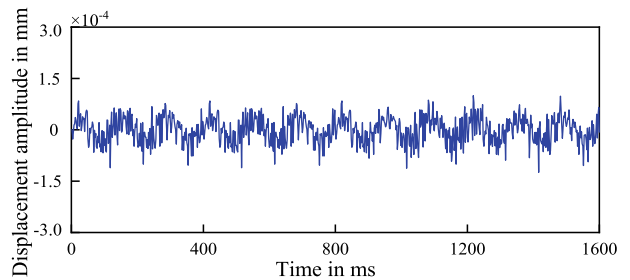


Fig. 14 Simulated curve of radial vibration displacement at point **a** under the no-load condition

are added. In the model of Fig. 12b, fixed constraints at the bottom corner of the prototype are added. The model in Fig. 12a is simulated to obtain stator vibration modes under no-load and rated-load conditions, as shown in Fig. 13. The model in Fig. 12b is established to capture the vibration curves at point **a** under two working conditions. Only the no-load working condition curve is shown in Fig. 14 due to the article length limitation.

Figure 13 shows that F_r and M_r make the stator core fluctuate six times based on the original model for both no-load and rated-load conditions, which means that the stator vibration mode is 6. The result is consistent with theoretical analysis result. In theoretical analysis, $Z_p = 6$, $\alpha_1 = 4$ for the 36-slot/6-pole combination. It is judged that the bending moments are in phase, and M_r is the main excitation source, so the vibration mode is $2p = 6$. To further explore the vibration mode law in Fig. 11b, c, and d, three motors with different slot/pole combinations are selected, i.e., 36/6, 12/8, and 36/8. The FE simulation results are shown in Table 5, which are compatible with the theoretical derivation in Table 4. The above analysis further illustrates the rationality of the equivalence, the correctness of the theoretical analysis model, and the applicability to both no-load and rated-load conditions.

Under the constant consumption of PM and polar arc coefficient, the V-shaped PM arrangement motor replaces the I-shaped one. The two-dimensional model

Table 5 Vibration mode law of three motors with different slot/pole combinations

Slots number	Poles number	Z_p	α_1	Vibration mode	
				Theoretical analysis	Simulation analysis
36	6	6	4.5	0	
12	8	1.5	1	4	
36	8	4.5	3.5	4	

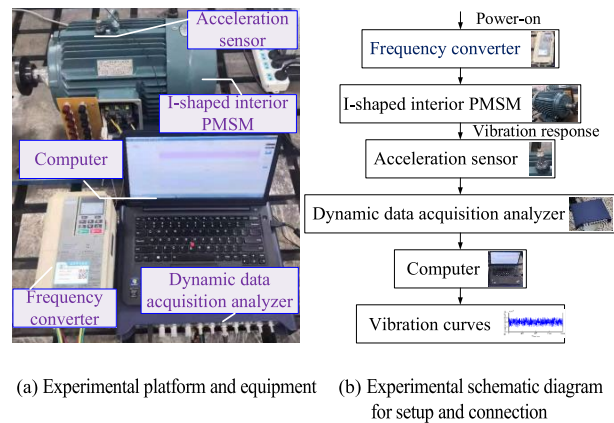


Fig. 17 The **a** experimental platform and equipment and **b** experimental schematic diagram for setup and connection

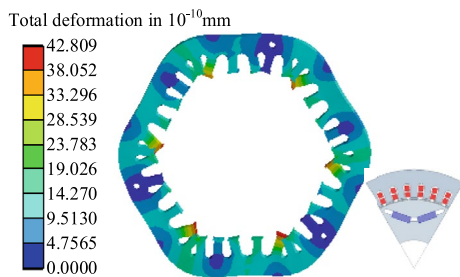


Fig. 15 Stator vibration mode of the V-shaped PM arrangement motor

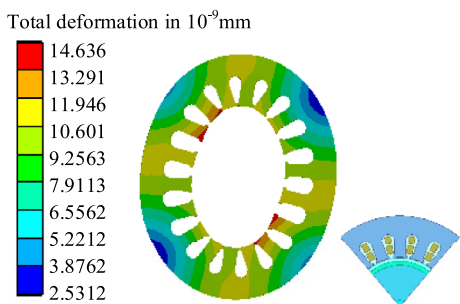


Fig. 16 Stator vibration mode of surface-mounted PMSM

and simulation results are shown in Fig. 15. As shown in Fig. 15, the stator vibration mode of the V-shaped PM arrangement motor is 6, which is compatible with that of the I-shaped one, indicating the applicability of the theoretical analysis model.

PMSM can be divided into interior and surface-mounted types. The section takes an 18/4 surface-mounted motor ($Z_p = 4.5$, $\alpha_1 = 4.5$) as the research object

to study the vibration mode law. The simulation result is presented in Fig. 16. It is identical to theoretical analysis, demonstrating the applicability of this scheme to a surface-mounted PMSM.

Experimental Verification of the Vibration Mode

This section deals with the experimental validation of stator vibration mode through vibration displacement amplitude. The experimental platform is described in Fig. 17a, and the equipment parameters are shown in Table 6. After power-on, the frequency converter controls the motor to start until running stably, and the vibration response is captured by ICP unidirectional acceleration sensor and imported into AVANT MI-7008 dynamic data acquisition analyzer for further analysis. Figure 17b shows the experimental setup and connection schematic diagram.

Since the prototype is three-phase symmetrical, all pairs of points between *a*, *b*, and *c* have the same stator vibration mode. This section only studies points *a*, *b*, and the central areas. The test indicates that 12 points can be continuously selected as measuring points on the central axis, as shown in Fig. 18.

The unidirectional acceleration sensor should be radially placed on the radiating fin during vibration measurement. After the stable operation, the acceleration sensor collects the vibration displacement of each measuring point. To save space, this paper only lists the vibration displacement curve at point *a* under no-load condition, as shown in Fig. 19.

Figures 14 and 19 show that the radial vibration displacement amplitude of the simulated curve is smaller than that of the experimental one due to the ideal simulation environment. However, the experimental environment should consider the EM and mechanical vibrations, equipment

Table 6 Main equipment parameters

Equipment	Parameter	Value
I-shaped interior PMSM	Rated power	3 kW
Frequency converter	Maximum output frequency	400 Hz
Dynamic data acquisition analyzer	Maximum sampling frequency	192 kHz
ICP type acceleration sensor	Sensitivity	100 mV/g
Computer	–	–

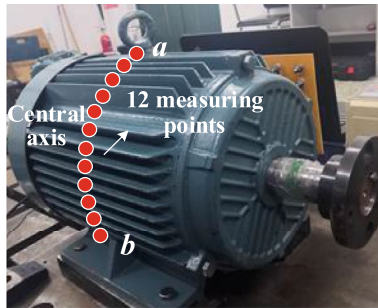


Fig. 18 Distribution of 12 continuous vibration measuring points along the central axis between points *a* and *b*

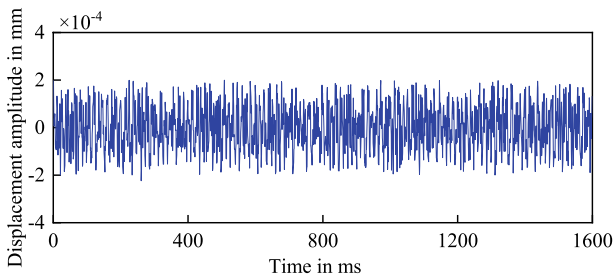


Fig. 19 Experimental curve of radial vibration displacement at point *a* under no-load condition

installation and fixation and other factors. Thus, the experimental displacement result is larger than the simulated one.

To further investigate the radial vibration displacement of 12 measuring points, the Fourier decomposition method performs frequency spectrum analysis on each point. Figure 20 compares the simulated and experimental frequency spectrum analysis at point *a* under the no-load condition. As shown in Fig. 20, simulated and experimental curves have the same trend. Besides, the radial vibration amplitude corresponding to 75 Hz is the largest, which can be an ideal reference point. The simulated and experimental displacement amplitude of 12 reference points between *a* and *b* is collected, as shown in Fig. 21.

As shown in Fig. 21, the overall trend of the simulated and experimental radial vibration displacement amplitude of 12 reference points is consistent. Moreover, Fig. 21 shows two stator core fluctuations between points *a* and *b*, leading

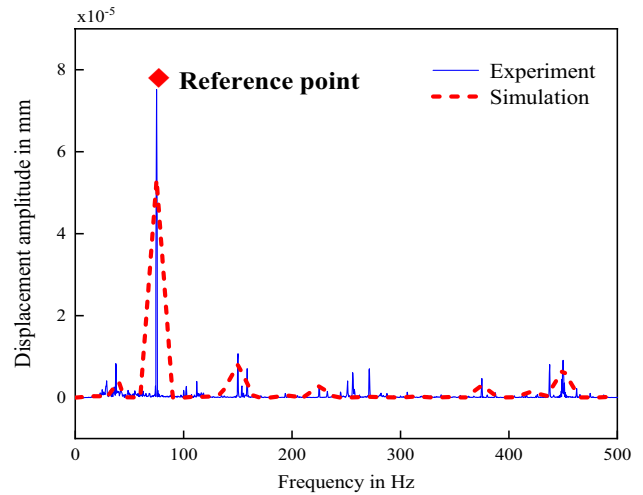


Fig. 20 Comparison of simulated and experimental frequency spectrum analysis at point *a* under no-load condition

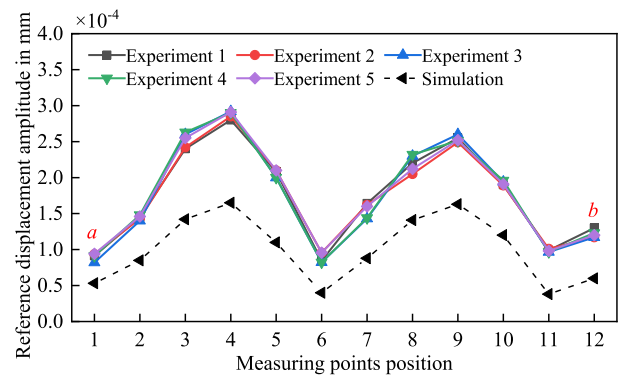


Fig. 21 The fluctuation curves of simulated and experimental radial vibration displacement amplitude of 12 reference points

two fluctuations between *b* and *c*, and *c* and *a*. Thus, the motor stator fluctuates six times. According to Fig. 21, the displacement amplitude of each reference point on the central axis of the motor is drawn in Fig. 22 to more intuitively analyze the vibration mode, where the experimental curve is the average value of five data groups. In Fig. 22, convex points of the simulated and experimental curves are connected for the convenience of analysis. The two connecting

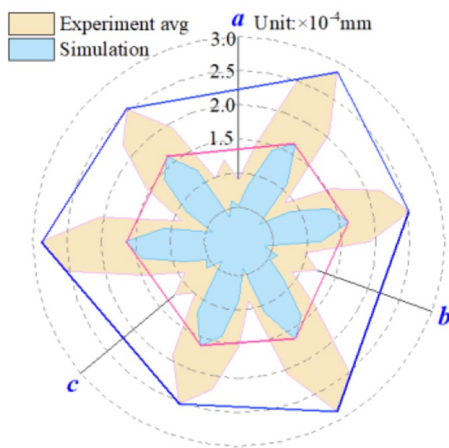


Fig. 22 The simulated and experimental radial vibration displacement amplitude distribution and vibration mode of the motor

lines have a hexagon shape; that is, their vibration modes are 6. Besides, the shape of the simulated connecting line is relatively symmetrical due to the ideal environment, while there are some errors in the experiment. Through curve fitting and comparison, the maximum error of simulation and experiment is calculated as 7.41%. This is mainly due to the gravity component of the acceleration sensor and radial installation error caused by radiating fins in the experiment, while this does not affect the vibration mode results. Therefore, in the above analysis process, simulated and experimental results can further demonstrate the correctness of the theoretical analysis model.

Conclusion

This paper analyzes radial EM force waves and determines the low spatial order. The double equivalence of air-gap permeance and air-gap flux density is realized using the above conclusion. A theoretical analysis model mainly comprises the total concentrated force and additional bending moment. This model is applied to PMSM with CSSR and PMSM with SSCR to explore the vibration mode law validated by FE and experimental methods. The conclusions are as follows:

- (1) Low spatial order force waves such as (6, 2) and (0, 12) can cause considerable vibration and noise. Among them, (0, 12) is mainly generated by the interaction between the rotor magnetic field and the first-order tooth harmonic magnetic field. Compared with other tooth harmonics, the one is dominant.
- (2) The vibration mode is determined by the F_r and M_r , which are affected by Z_p and α_1 . Z_p determines whether bending moment phases on the teeth corresponding to

adjacent magnetic poles are in phase, and α_1 determines the excitation source attribute. When Z_p is an integer, the bending moment phases are the same; When Z_p is (integer + 0.5), the bending moment phases are opposite; When α_1 is an integer, the excitation source is M_r ; When α_1 is (integer + 0.5), the excitation source is F_r .

- (3) Z_p and α_1 are mainly affected by slot/pole combination, so the slot/pole combination indirectly affects the F_r and M_r , and its ratio plays an essential role in the vibration mode.
- (4) This paper proposes a theoretical analysis model suitable for both PMSM with CSSR and PMSM with SSCR to study the action law, causes, and influencing factors of stator vibration mode. It lays the foundation for the prediction and reduction of motor vibration.

Funding This work is supported by the National Natural Science Foundation of China under the Grant No. 51977052 and the Grant No. U21A20145, and the Natural Science Foundation of Heilongjiang Province under the Grant No. ZD2022E006.

Data availability The data that support the findings of this study are available from the corresponding author upon reasonable request.

Declarations

Conflict of Interest The authors declare that the research was conducted in the absence of any commercial or financial relationships that could be construed as a potential conflict of interest.

References

1. Zhang Z, Dong Y, Han Y (2020) Dynamic and control of electric vehicle in regenerative braking for driving safety and energy conservation. *J Vib Eng Technol* 8:179–197. <https://doi.org/10.1007/s42417-019-00098-0>
2. Gao MZ, Cai CP (2018) Fault-tolerant control for wing flutter under actuator faults and time delay. *J Vib Eng Technol* 6(6):429–439
3. Song Y, Liu Z, Hou R et al (2022) Research on electromagnetic and vibration characteristics of dynamic eccentric PMSM based on signal demodulation. *J Sound Vib*. <https://doi.org/10.1016/j.jsv.2022.117320>
4. Li S, Su Y, Shen C (2018) Noise analysis and control on motor starting and accelerating of electric bus. *J Vib Eng Technol* 6:93–99. <https://doi.org/10.1007/s42417-018-0019-2>
5. Deng W, Zuo S, Chen W, Qian Z, Qian C, Cao W (2022) Comparison of eccentricity impact on electromagnetic forces in internal- and external-rotor permanent magnet synchronous motors. *IEEE Trans on Transport Electrification* 8(1):1242–1254
6. Zhao J, Wang Z, Liu H, Ning F, Hong X et al (2020) Modal analysis and structure optimization of permanent magnet synchronous motor. *IEEE Access* 8:151856–151865
7. Hara T, Ajima T, Hoshino K, Ashida A (2020) Carrier electromagnetic vibration of DC voltage fluctuation in permanent-magnet

- synchronous motor with distributed winding. *IEEE Trans Ind Appl* 56(5):4623–4631
8. He C, Li S, Shao K et al (2022) Robust iterative feedback tuning control of a permanent magnet synchronous motor with repetitive constraints: a Udwadia-Kalaiba approach. *J Vib Eng Technol* 10:8394. <https://doi.org/10.1007/s42417-021-00365-z>
 9. Lin F, Zuo S, Deng W et al (2018) Reduction of vibration and acoustic noise in permanent magnet synchronous motor by optimizing magnetic forces. *J Sound Vib* 429:193–205. <https://doi.org/10.1016/j.jsv.2018.05.018>
 10. Zhu ZQ, Howe D, Bolte E, Ackermann B (1993) Instantaneous magnetic field distribution in brushless permanent magnet DC motors. I. Open-circuit field. *IEEE Trans Magn* 29(1):124–135
 11. Chen Y, Zhu Z, Howe D (2006) Vibration of permanent magnet brushless machines having a fractional number of slots per pole. In: 2006 IEEE International Magnetics Conference (INTERMAG), San Diego, CA, USA, pp 496–496
 12. Chai F, Li Y, Pei Y, Yu Y (2019) Analysis of radial vibration caused by magnetic force and torque pulsation in interior permanent magnet synchronous motors considering air-gap deformations. *IEEE Trans Ind Electron* 66(9):6703–6714
 13. Xu Y, Fang H, Li D, Qu R, Guo J (2020) Fast evaluation of high frequency electromagnetic force and vibration for PMSMs based on field reconstruction technique. *IEEE Trans Ind Appl* 56(4):3549–3558
 14. Xing Z, Zhao W, Wang X, Sun Y (2020) Reduction of radial electromagnetic force waves based on PM segmentation in SPMSMs. *IEEE Trans Magn* 56(2):1–7
 15. Jing L, Gong J, Zhang Y, Qu R (2020) Analytical calculation and design of magnetic variable speed permanent magnet brushless machine with halbach arrays. *Trans China Electrotech Soc* 35(5):954–962
 16. Jalali P, Boroujeni ST, Bianchi N (2017) Analytical modeling of slotless eccentric surface-mounted PM machines using a conformal transformation. *IEEE Trans Energy Convers* 32(2):658–666
 17. Wang X, He X, Gao P (2019) Research on electromagnetic vibration and noise reduction method of V type magnet rotor permanent magnet motor electric vehicles. *Proc CSEE* 39(16):4919–4926
 18. Lin F, Zuo S, Deng W, Wu S (2016) Modeling and analysis of electromagnetic force, vibration, and noise in permanent-magnet synchronous motor considering current harmonics. *IEEE Trans Ind Electron* 63(12):7455–7466
 19. Yang H, Chen Y (2014) Influence of radial force harmonics with low mode number on electromagnetic vibration of PMSM. *IEEE Trans Energy Convers* 29(1):38–45
 20. Valavi M, Le Besnerais J, Nysveen A (2016) An investigation of zeroth-order radial magnetic forces in low-speed surface-mounted permanent magnet machines. *IEEE Trans Magn* 52(8):1–6
 21. Islam MS, Islam R, Sebastian T (2014) Noise and vibration characteristics of permanent-magnet synchronous motors using electromagnetic and structural analyses. *IEEE Trans Ind Appl* 50(5):3214–3222
 22. Wang Qiu XA (2012) Finite element calculation of radial electromagnetic force wave in squirrel-cage asynchronous motors. *Trans China Electrotech Soc* 27(7):109–117
 23. Lee S-H, Yang I-J, Kim W-H, Jang I-S (2021) Electromagnetic vibration-prediction process in interior permanent magnet synchronous motors using an air gap relative permeance formula. *IEEE Access* 9:29270–29278
 24. Hara T, Ajima T, Tanabe Y, Watanabe M, Hoshino K, Oyama K (2018) Analysis of vibration and noise in permanent magnet synchronous motors with distributed winding for the PWM method. *IEEE Trans Ind Appl* 54(6):6042–6049
 25. Jang I, Kim W (2020) Study on electromagnetic vibration analysis process for PM motors. *IEEE Trans Appl Supercond* 30(4):1–6
 26. Wang S, Hong J, Sun Y, Cao H (2018) Exciting force and vibration analysis of stator permanent magnet synchronous motors. *IEEE Trans Magn* 54(11):1–5
 27. Wu Z, Zuo S, Huang Z et al (2022) Modelling, calculation and analysis of electromagnetic force and vibroacoustic behavior of integer slot permanent magnet synchronous motor considering current harmonics. *J Vib Eng Technol* 10:1135–1152. <https://doi.org/10.1007/s42417-022-00434-x>

Publisher's Note Springer Nature remains neutral with regard to jurisdictional claims in published maps and institutional affiliations.

Springer Nature or its licensor (e.g. a society or other partner) holds exclusive rights to this article under a publishing agreement with the author(s) or other rightsholder(s); author self-archiving of the accepted manuscript version of this article is solely governed by the terms of such publishing agreement and applicable law.